



Semi-microscopic analysis of $^{20}\text{Ne} + ^{130}\text{Te}$ elastic and inelastic scattering at 15.3 A MeV

Kassem O. Behairy¹  M. A. Hassanain² M. Anwar¹ A. Hemmdan^{1†} 

¹Physics Department, Aswan University, Aswan 81528, Egypt

²Physics Department, New-Valley University, El-Kharga, Egypt

Abstract: The new measured data of elastic and inelastic $^{20}\text{Ne} + ^{130}\text{Te}$ scattering at an energy of 15.3 A MeV are analyzed in framework of the nuclear optical potential. Three types of semi-microscopic potentials are used: the real part is calculated using a double folding model in conjunction with the conventional phenomenological Woods-Saxon (WS) potential for the imaginary part. Two real cluster models are constructed using the cluster structure of ^{20}Ne nucleus as 5α and $\alpha + ^{16}\text{O}$. The real part of the third potential is generated using a CDM3Y6 interaction employed for comparison. Three excited energies to the superposition of the projectile and target states, ground-state (Quasi), 1.6 and 2.5 MeV are investigated using deformed potentials. The contributions of these states are calculated using a one-step distorted wave Born approximation and coupled Channels approaches. Successful calculations and results using semi-microscopic potentials in simple one-channel and coupled channels are obtained. The values of cross section and volume integrals require more contributions to enable more comparisons regarding this project.

Keywords: nuclear reactions, optical model, elastic and inelastic scattering, coupled channels, folding model, cluster structure, double charge exchange reactions.

DOI: 10.1088/1674-1137/ad9305 **CSTR:** 32044.14.ChinesePhysicsC.49044109

I. INTRODUCTION

The physics community is interested in investigating whether neutrinos are Majorana fermions. Neutrinoless double beta decay ($0\nu\beta\beta$) is the most auspicious resource for providing a precise measurement of the effective neutrino mass and establishing the Majorana and Dirac nature of the neutrino [1, 2]. However, this decay is still a predicted and unobserved spontaneous decay that awaits experimental confirmation. This phenomenon could provide valuable information to interpret key problems of fundamental physics, such as the unification of the fundamental forces and the matter-antimatter balance in the universe [3–6]. A few nuclei are known to decay via this rare process, as discussed in Refs. [7, 8].

A critical aspect of $0\nu\beta\beta$ physics is associated with the determination of the Nuclear Matrix Elements (NMEs) entering the expression of the decay half-life [1, 9]. These quantities must be known with good accuracy, despite the intrinsic many-body nature of the parent and daughter nuclei, which makes this task particularly difficult. No experimental methods can directly measure $0\nu\beta\beta$ NMEs, and state-of-the-art theoretical calculations lead to discrepancy factors larger than 2 [10]. In addition, some assumptions that are common to different nuclear struc-

ture approaches can cause systematic uncertainties. Thus, experimentally driven inputs relevant to understanding the $0\nu\beta\beta$ responses are useful for evaluating the $0\nu\beta\beta$ NMEs constraining existing calculations [11–17].

In this context, experimentalists and theorists are undertaking significant efforts to study heavy-ion induced single charge exchange (SCE) and double charge exchange (DCE) reactions [18–21] to identify possible connections with $0\nu\beta\beta$ [18], whereas other complementary studies [22, 23] have recently explored DCE reactions in connection to $0\nu\beta\beta$ and populate exotic structures. Moreover, the precise determination of the NMEs of the surrogate process requires measuring all the reaction channels characterized by the same initial projectile and target nuclei. Therefore, experimental projects aim to investigate the complete net of reaction channels, including not only DCE and SCE but also transfer reactions and elastic and inelastic scattering channels [24].

From a theoretical perspective, the description of the measured DCE cross sections poses significant challenges. This requires a detailed microscopic description of the reaction mechanism. The state-of-art reaction theory for the description of SCE and DCE reactions up to high excitation energies triggers the need for knowledge of the initial and final state interactions for these scatter-

Received 3 August 2024; Accepted 13 November 2024; Published online 14 November 2024

[†] E-mail: ahemdan@aswu.edu.eg

©2025 Chinese Physical Society and the Institute of High Energy Physics of the Chinese Academy of Sciences and the Institute of Modern Physics of the Chinese Academy of Sciences and IOP Publishing Ltd. All rights, including for text and data mining, AI training, and similar technologies, are reserved.

ing systems.

Promising experiments are being conceived by searching for the $0\nu\beta\beta$ decay in nuclei reactions such as ^{48}Ca , ^{76}Ge , ^{116}Cd , ^{130}Te , and ^{136}Xe , with half-lives higher than 10^{25}y [4–6]. One of the heaviest targets explored to date in the NUMEN project is the ^{130}Te nucleus [25–27]. The CUORE [27] and SNO+ [28] experimental campaigns are seeking to measure the $0\nu\beta\beta$ half-life for this nucleus and provide an experimental limit for the $0\nu\beta\beta$ half-life. The $^{20}\text{Ne}+^{130}\text{Te}$ system, theoretically investigated in this article, was studied for the first time within NUMEN [24, 25]. In this first work, the elastic and inelastic scattering cross-section angular distributions of this system were measured, and a theoretical analysis was performed using the optical model [25]. Coupled-channel (CC) approaches and one-step distorted wave Born approximation (DWBA) using the São Paulo double-folding (DF) optical potential were used in the calculations. A satisfactory description of the experimental data in the entire explored range was obtained, provided that couplings with the 2^+ states of the projectile and target were explicitly included within the CC technique.

The optical model is one of the important models describing the DCE mechanism. In this model, the optical potential has a central role, as it describes the average interaction during the collisions between the nuclei involved in the entrance and exit partitions. Information regarding the optical model potential (OMP) for such reactions has not been thoroughly tested. Thus, this task requires the control of the distortions of the incoming and outgoing waves owing to the OMPs, as shown in Refs. [29–31]. Another option is to derive an OMP from the DF of a realistic nucleon–nucleon (NN) interaction with the matter densities of the projectile and target nuclei [32]. This was also performed in our previous papers [33–37]. In some cases, specific models, such as the cluster one [38–43], can be adopted, as recently performed for the $^{20}\text{Ne}+^{76}\text{Ge}$ system at 306 MeV in our recent work [44].

The present article is an extension to the previous one [44] to analyze the complete net of elastic and inelastic scattering channels of the new experimental data of the $^{20}\text{Ne}+^{130}\text{Te}$ interaction. The target ^{130}Te nucleus is a candidate nucleus for $0\nu\beta\beta$ decay [25], and limited theoretical analyses have been presented in the literature regarding the $^{20}\text{Ne}+^{130}\text{Te}$ reaction. Furthermore, these data provide opportunities to confirm our theoretical calculations and nuclear structure models of the reaction nuclei used for heavy ion (HI) reactions. This paper is considered a contribution to this field.

Therefore, the main objective of this article is to reconfirm the ability of the three calculated OMPs using the same procedures as in Ref. [44] to reproduce the considered data. The two-cluster potential model is generated based on the like α cluster (5α cluster) [45–47] and

the unlike α cluster ($\alpha+^{16}\text{O}$) [48] of the ^{20}Ne nucleus to present a description of the data for elastic and inelastic $^{20}\text{Ne}+^{130}\text{Te}$ scattering at 15.3 A MeV [25]. The third potential model is the CDM3Y6 effective NN interaction [49, 50] for comparison; it is dependent on the density and energy and has been proved to be effective in most folding calculations. Additionally, the relevant internal states (inelastic channels) of the projectile-target system are properly considered using DWBA and CC techniques for a complete understanding of the scattering dynamics of the reaction under study.

The remainder of this paper is organized as follows: A brief description of the derived formalisms is given in Sect. II. Section III presents the results and discussion. Finally, conclusions are given in Sect. IV.

II. THEORETICAL FORMALISM

Most of the studied HI scattering data showed that they are sensitive to the potential at the long-range radius, and the dominant contributions of the potential result from the surface and tail regions of the nuclear densities. One of the constructed potentials that can reproduce the observed HI elastic and inelastic scattering for many systems with long ranges of bombarding energies is the semi-microscopic potential [44, 51, 52]. The total semi-microscopic nuclear potential of the $^{20}\text{Ne}+^{130}\text{Te}$ system in this work is used in the form

$$U(R) = N_R V(R) + iW_0 \left[1 + \exp\left(\frac{R-R_W}{a_W}\right) \right]^{-1} + V_C(R), \quad (1)$$

where $V_C(R)$ is the Coulomb potential, taken as a uniformly charged sphere of radius $R_C = 1.2(A_T^{1/3} + A_P^{1/3})$, and A_T and A_P are the masses of the target and projectile, respectively. The second term represents the imaginary part, because the parameters W_0 , R_W , and a_W are the depth, radius, and diffuseness of the imaginary potential, respectively. The radius is calculated as $R_W = r_w (A_T^{1/3} + A_P^{1/3})$. The first term represents the real part ($V(R)$) of the OMP. The N_R factor is multiplied by the potential model to optimize the fit to the experimental data; if the value $N_R \approx 1.0$, this indicates success for the model, whereas any systematic deviation of N_R from unity requires a correction to the calculated potential. The real part $V(R)$ is calculated using three different DF model forms:

$$V(R) = \iint \rho_{Ne}(\mathbf{r}_1) \rho_{Te}(\mathbf{r}_2) v_{NN}(s) d\mathbf{r}_1 d\mathbf{r}_2, |s| = |\mathbf{R} - \mathbf{r}_1 + \mathbf{r}_2|. \quad (2)$$

The three calculated DF models depend on different forms of the density distributions of the projectile ^{20}Ne and target ^{130}Te nuclei and the NN effective $v_{NN}(s)$ inter-

actions. Three different forms of densities, two cluster structure of ^{20}Ne nucleus as unlike α cluster $\alpha + ^{16}\text{O}$ with the wave function for the relative motion of the α and ^{16}O clusters in the ground state $\psi(r)$ and the like α cluster (5α), in addition to the form of the Fermi–density distribution density (2pF) [53, 54] for both ^{20}Ne and ^{130}Te nuclei, are taken. Additionally, three types of $v_{NN}(s)$ interactions are used. Their parameters and details of calculation procedures are defined and explained in Refs. [44, 55, 56]. The 2pF form of the target ^{130}Te nucleus is taken as [53, 54]

$$\rho_{\text{Te}}(r) = \rho_0 \left[1 + \exp\left(\frac{r-r_c}{0.55}\right) \right]^{-1}, \quad (3)$$

Therefore, the calculated OMPs within the first order calculations generated using Eqs. (1)–(3) are CPM1, CPM2, and CDM3Y6 as follows:

$$V_{\text{CPM1}}(R) = \int \left[V_{\alpha\text{-Te}}\left(\mathbf{R} - \frac{4}{5}\mathbf{r}\right) + V_{\text{O-Te}}\left(\mathbf{R} + \frac{1}{5}\mathbf{r}\right) \right] |\psi(r)|^2 d\mathbf{r}, \quad (4)$$

$$V_{\alpha\text{-Te}}(r) = \int \rho_{\text{Te}}(\mathbf{r}') v_{\alpha N}(|\mathbf{r} - \mathbf{r}'|) d\mathbf{r}',$$

$$V_{\text{O-Te}}(r) = \int \rho_{\text{O}}(\mathbf{r}_1) \rho_{\text{Te}}(\mathbf{r}_2) v_{NN}(s) d\mathbf{r}_1 d\mathbf{r}_2, s = |\mathbf{r} - \mathbf{r}_1 + \mathbf{r}_2|$$

$$V_{\text{CPM2}}(R) = \iint \rho_{\text{Ne}}^{\text{C}}(\mathbf{r}_1) \rho_{\text{Te}}(\mathbf{r}_2) v_{\alpha N}(s) d\mathbf{r}_1 d\mathbf{r}_2, \quad (5)$$

$$V_{\text{CDM3Y6}}(R) = \iint \rho_{\text{Ne}}(\mathbf{r}_1) \rho_{\text{Te}}(\mathbf{r}_2) v_{NN}(s) d\mathbf{r}_1 d\mathbf{r}_2 \quad (6)$$

Second, in the theoretical formalism to evaluate the deformed potential (DP) model for studying the inelastic $^{20}\text{Ne} + ^{130}\text{Te}$ scattering, the calculations of the inelastic channels are performed using the one-step DWBA and CC approaches within the DP in the context of the rotational model. This DP, the nuclear coupling potential, is directly extracted as a derivative of the adapted elastic CPM1 potential to analyze the inelastic channels. The DP potential is given as

$$U_{\lambda}^{\text{DP}}(r) = -\frac{1}{\sqrt{4\pi}} \delta_{\lambda}^U dU_{\text{CPM1}}(r)/dr, \quad U = W, R. \quad (7)$$

The coupling potentials in macroscopic models are often expressed in terms of multiple decomposition as in Eq. (7) for the multipolarity $\lambda \geq 2$ [57]. While δ_{λ}^U is the potential deformation length that determines the strength of the interaction, it corresponds with the electric transition probabilities $B(E\lambda \uparrow)$ [58]. The transition probabilities can only be extracted from the measured cross sections when the contributions from both the Coulomb and nuclear interactions to the total cross section are correctly accounted for. $\delta_{\lambda}^R = \delta_{\lambda}^W = \beta_{\lambda} R$, where β_{λ} is the deformation parameter, and R is the radius of the deformed potential for real part (R) or imaginary part (W). The deformation parameter is determined by

$$\beta_{\lambda} = \frac{4\pi}{3ZR^2} [B(E\lambda; I \rightarrow I') b^2 e^2 / e^2]^{1/2}. \quad (8)$$

The corrected deformation length ($\delta_{\lambda}^{\text{corr}}$) of the heavy nuclear reactions is adopted for the deformed potential to consider the relative differences in the density and potential radius, as follows [25, 44]:

$$\delta_{\lambda}^{\text{corr}} = \delta_{\lambda} R / R_{\text{pot}}, \quad (9)$$

where the radius R_{pot} of the considered potentials is listed in Table 1. In this work, the deformed CPM1 potential is generated to study the quasi-elastic and inelastic scattering. Therefore, the complex inelastic OMP will be in the form

$$U_{\text{DP}}^{\lambda}(R) = V_{\lambda}^{\text{C}}(R) + U_{\lambda}^{\text{CPM1}}(R). \quad (10)$$

III. RESULTS AND DISCUSSION

This paper analyzes and studies the reaction mechanism of the quasi-elastic and inelastic of $^{20}\text{Ne} + ^{130}\text{Te}$ scattering. The role of the initial-state interaction (ISI) and final-state interaction (FSI) is fundamental to studying all the nuclear reaction channels in the theoretical description of reactions mechanism. In the same context, the OPs

Table 1. Parameters required for best fit of $^{20}\text{Ne} + ^{130}\text{Te}$ system at 15.3 A MeV using OMPs. The parameters N_R , r_w , and a_w are fixed at 1.0, 1.40, and 0.55 fm, respectively.

Pot.	W_0/MeV	$J_R/(\text{MeV}\cdot\text{fm}^3)$	$(r_R^2)^{1/2}/\text{fm}$	$J_W/(\text{MeV}\cdot\text{fm}^3)$	$(r_W^2)^{1/2}/\text{fm}$	χ^2	σ_R/mb
CPM1	9.17	368.2	5.92	19.60	8.68	2.8	3389
CPM2	16.42	370.6	6.08	35.04	8.68	5.8	3636
CDM3Y6	16.64	377.0	6.27	35.04	8.68	6.2	3639

represent an important tool for describing the ISI and FSI. Therefore, three semi-microscopic OPs models are used: two cluster models, CPM1 and CPM2, and the nucleonic potential of the CDM3Y6 density-energy dependent effective NN interaction. The three considered real potentials are evaluated using our computer code [59] and DFPD4 computer code [60].

The radial shape of the three potential models for the $^{20}\text{Ne}+^{130}\text{Te}$ reaction is shown in Fig. 1, in linear (Panel (a)) and logarithmic (Panel (b)) scales. The strong absorption radius is 5.61 ± 0.02 fm, approximately for the potentials, as indicated by the arrows in the two panels. We observe from Fig. 1 that the three potentials, CPM1, CPM2, and CDM3Y6, generally have the same behavior. Additionally, these potentials have the following characteristics: CPM1 is deeper at small radii and steeper than the other two potentials at large radii owing to the cluster structure of the ^{20}Ne nucleus, and the nucleonic CDM3Y6 potential is steeper than the other two potentials at small radii ($\approx 80.1\%$ from average other two potentials). These characteristics of CPM1 are consistent with those of previous studies [44], inclusive of the nucleonic CDM3Y6 potential of [44] and the real nuclear SSP potential of [25]. Moreover, the cluster potentials provide good results for the χ^2 value as given in Table I compared with

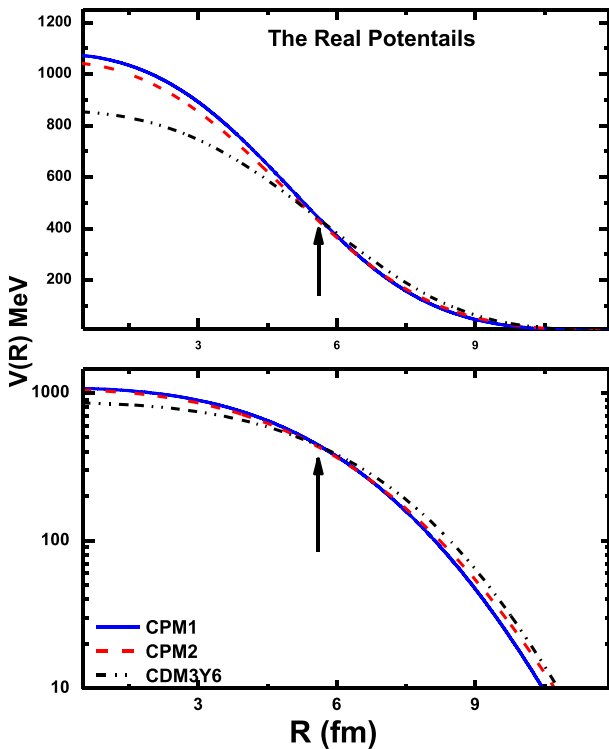


Fig. 1. (color online) Three real OMPs of the $^{20}\text{Ne}+^{130}\text{Te}$ reaction: panel (a) for linear scale and panel (b) for logarithmic scale. In the curves of the potentials, the continuous, dashed, and dash double dotted lines are for CPM1, CPM2, and CDM3Y6, respectively.

the nucleonic CDM3Y6 potential. These calculated OMPs, in addition to the extracted DP, are used in the analysis of the experimental data under study.

The experimental data considered in this work are obtained from Ref. [25]. Three types of measured experimental data are extracted from the excitation energy spectrum for the ^{130}Te ($^{20}\text{Ne}, ^{20}\text{Ne}$) ^{130}Te scattering at an incident energy of $15.3 A$ MeV and $16.8^\circ < \theta_{\text{lab}} < 17.2^\circ$. These data identify three peaks corresponding to the superposition of the projectile and target states: the quasi elastic scattering, with expected contributions to the cross-section from the 2^+ excited state of ^{130}Te at 0.839 MeV, which is not separated from the elastic peak owing to the energy resolution; the second peak at ≈ 1.6 MeV, corresponding to the population of the $\text{Ne}_{1,633}^{+2} + \text{Te}_{\text{g.s.}}^{+0}$ and $\text{Ne}_{\text{g.s.}}^{+0} + \text{Te}_{1,632}^{+4}$, and third peak at ≈ 2.5 MeV, with the expected contribution of the $\text{Ne}_{1,633}^{+2} + \text{Te}_{0,839}^{+2}$ transition.

The theoretical calculations of the cross section angular distribution using the optimized OMP and DP potentials are obtained using the FRESKO Computer Code [61]. Many attempts have been undertaken for auto searches to measure the ability of the elastic OMP and inelastic DP potentials as acceptable fits of the quasi-elastic and inelastic scattering for system under study. Therefore, the values of imaginary potential radius (r_w) and diffuseness (a_w) are fixed. Finally, the procedures in this work optimize one free parameter, the depth (W_0) of the WS imaginary part. The same procedure for the elastic calculations is used in the inelastic cross section while keeping the value of $\delta_\lambda^{\text{corr}}$ fixed. The experimental data are fitted by minimizing the χ^2 value, defined as

$$\chi^2 = \frac{1}{N} \sum_{k=1}^N \left[\frac{\sigma_{\text{th}}(\theta_k) - \sigma_{\text{ex}}(\theta_k)}{\Delta\sigma_{\text{ex}}(\theta_k)} \right]^2. \quad (11)$$

σ_{th} (σ_{ex}) is the theoretical (experimental) cross section at an angle θ_k in the c.m. system, $\Delta\sigma_{\text{ex}}$ is the experimental error, and N the number of the data points.

Therefore, the experimental angular distribution of $^{20}\text{Ne}+^{130}\text{Te}$ quasi-elastic and inelastic scattering at 15.3 A MeV is analyzed using the derived semi-microscopic OMPs and DP for CPM1, respectively. Comparisons of the experimental data with the theoretical prediction of the cross section are shown in Figs. 2–5. The best-fit parameters required for best fit are listed in Tables 1–2.

As shown in Table 2, the obtained real potentials with $N_R = 1.0$, in addition to the limited variation of one parameter, W_0 , of the WS imaginary part validates our model compared with the model used in Ref. [25].

The resulting angular cross sections using the three derived potentials of $^{20}\text{Ne}+^{130}\text{Te}$ elastic scattering at 15.3 A MeV are comparable to the experimental data. The best-fit parameters are listed in Table 1 and shown in Fig. 2. We observe a reasonable agreement with the experi-

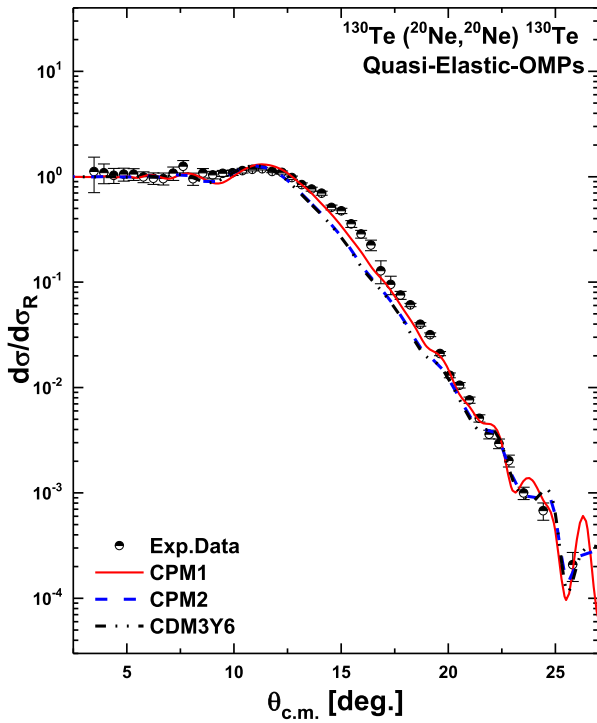


Fig. 2. (color online) Comparison of the data of the quasi-elastic angular distribution [25] for $^{20}\text{Ne} + ^{130}\text{Te}$ scattering at 15.3 A MeV and the theoretical predictions obtained using the OMPs in a simple one-channel (CPM1, CPM2, and CDM3Y6), shown as solid, dashed, and dashed double dotted lines, respectively.

mental data from Fig. 2 and Table I for the OMPs of the cluster density and the comparison potential, CDM3Y6. This figure shows that the calculated cluster CPM1 potential leads to a satisfactory prediction of the elastic scattering cross sections over most of the measured angular range for the $^{20}\text{Ne} + ^{130}\text{Te}$ system. Moreover, in the angular range $\theta \approx 13^\circ - 20^\circ$, CPM1 has almost the best fitting with the data and the smallest χ^2 value compared with the other potentials (CPM2 and CDM3Y6). This may be owing to the cluster structure ($\alpha + ^{16}\text{O}$) of ^{20}Ne , which contributes to the deformation of the nucleus geometric structure [44]. In addition, observing CPM1 in Fig. 2, the agreement between the experimental data and the present calculations appears correspond with the results of the folded São Paulo potential (SPP) in Ref. [25].

We investigate the contribution of the excited states of the projectile and target for $^{130}\text{Te} (^{20}\text{Ne}, ^{20}\text{Ne})^{130}\text{Te}$ scattering, which is expected in this energy region. The contribution of the 2^+ excited state of ^{130}Te at 0.839 MeV in quasi-elastic scattering is considered. The $\text{Ne}_{1.633}^{+2} + \text{Te}_{\text{g.s.}}^{+0}$ and $\text{Ne}_{\text{g.s.}}^{+0} + \text{Te}_{1.632}^{+4}$ transition in the second energy peak of the spectrum is tested. Finally, the $\text{Ne}_{1.633}^{+2} + \text{Te}_{0.839}^{+2}$ transition in the third excited state is calculated. The theoretical cross-section angular distribution calculations are performed within the one-step DWBA and CC approaches

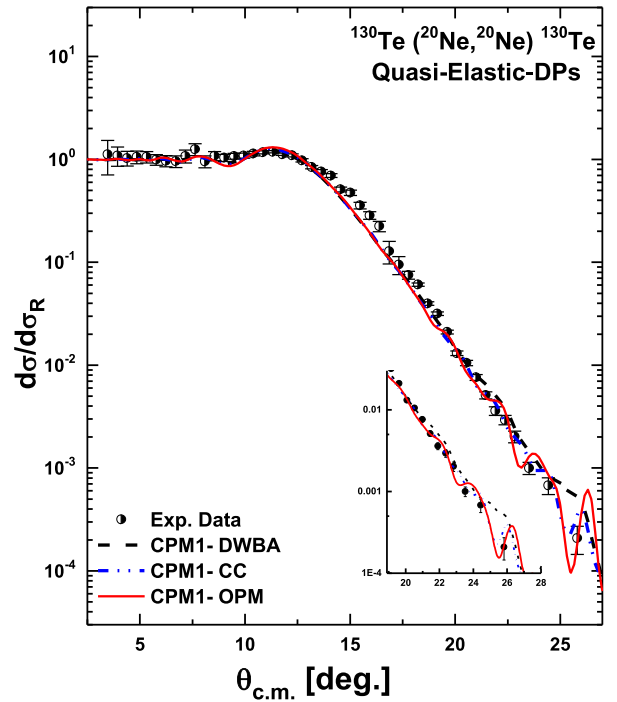


Fig. 3. (color online) Same as Fig. 2 but for CPM1 using the total contributions from the 2^+ excited state of ^{130}Te at 0.839 MeV ($\text{Te}_{0.839}^{+2}$). The $\text{Te}_{0.839}^{+2}$ for the one-step DWBA and CC approaches are represented by the dashed and dash double dotted lines, respectively, compared with the OPM of CPM1 as a solid line. The overlapping between the curves in large angles is shown in the inset.

based on the sketch in Figure 6 (Panel(a)) of Ref. [25]. Some coupling states far from providing any successful calculations in the previous study in Ref. [25] using the DP are neglected, as in Eq. (7). The deformed potential is calculated for the adopted OMPs of the simple one-channel using a corrected deformation length as in Eq. (8) to consider the relative differences in the density and radius of the OMP (R_{pot}). The results of R_{pot} are listed in Table I and are consistent with the results of Refs. [25, 57] with a slight difference. This provides a reasonable description of the optical potential properties.

The theoretical prediction of CPM1 of the simple one-channel, in addition to the total one-step DWBA and total CC calculations of the target excitation at 0.839 MeV ($\text{Te}_{0.839}^{+2}$) in ^{130}Te for the quasi-elastic data, is shown in Fig. 3. The data and calculations, particularly at large angles ($\theta > 20^\circ$), agree closely when the coupling with the second 2^+ state ($\text{Te}_{0.839}^{+2}$) is considered in the CC approach than others (DWBA and OMPs).

The contribution of the $\text{Ne}_{1.633}^{+2} + \text{Te}_{\text{g.s.}}^{+0}$ and $\text{Ne}_{\text{g.s.}}^{+0} + \text{Te}_{1.632}^{+4}$ transition states are included in the cross-section angular distribution calculations of the inelastic scattering at 1.6 MeV using the one-step DWBA and CC technique as shown in Fig. 4. The theoretical inelastic cross-section in Fig. 4 shows that the present results and data agree

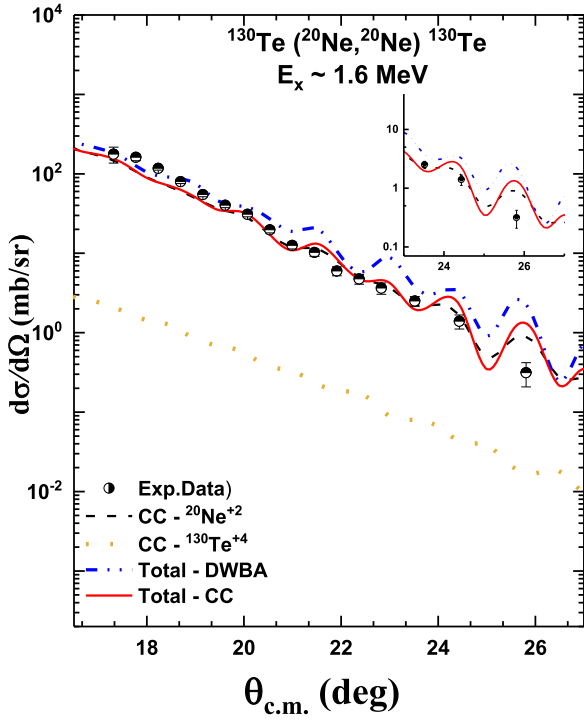


Fig. 4. (color online) Comparison of the experimental data of the inelastic $^{20}\text{Ne}+^{130}\text{Te}$ scattering with the theoretical prediction of the DWBA and CC calculations at $15.3A$ MeV. The inelastic experimental data identify the second peak corresponding to the superposition of the projectile and target states at 1.6 MeV [25]. The theoretical predictions of the $\text{Ne}_{1.633}^{+2} + \text{Te}_{\text{g.s.}}^{+2}$ and $\text{Ne}_{\text{g.s.}}^{+0} + \text{Te}_{1.632}^{+4}$ transitions are shown as dashed lines. The dash double dotted line represents the total DWBA transition, whereas the solid line represents the total CC calculations.

closely when the $\text{Ne}_{1.633}^{+2}$ state is included or when the full coupling effects are considered in the CC approach. These results illustrate the importance of including the excited state of $\text{Ne}_{1.633}^{+2}$ in reproducing the data. These results are consistent with previous studies [25, 44, 62].

The analysis of the third inelastic scattering data at 2.5 MeV using the $\text{Ne}_{1.633}^{+2} + \text{Te}_{0.839}^{+2}$ transition in the CC calculations is shown in Fig. 5. The calculated angular distribution cross section of the considered potential (CPM1) is fitted the experimental data more than that obtained in Figure 4 (b) in Ref. [25]. This result may be owing to the

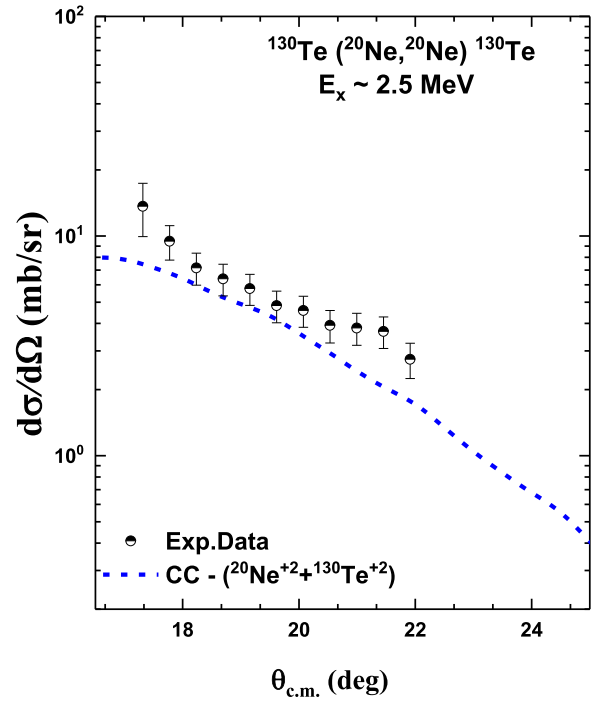


Fig. 5. (color online) Same as Fig. 4., but for the third visible peak at 2.5 MeV of the $^{20}\text{Ne}+^{130}\text{Te}$ system [25]. The dashed line represents the results of the theoretical prediction of the CC calculations for $\text{Ne}_{1.633}^{+2} + \text{Te}_{0.839}^{+2}$ transitions.

semi-microscopic potential and cluster density of the projectile ^{20}Ne in this work.

The normalization factor (N_R), real volume integrals (J_R), and total reaction cross section (σ_R) are important physical quantities that characterize the optical potential properties. These quantities are listed in Tables 1–2. The difference between the present J_R of CPM1 and the resulting J_V of SPP in Ref. [25] is approximately 8%. This value is the smallest percentage of the three OPs listed in Table 1. This indicates that CPM1 is preferred in describing such studied systems.

IV. CONCLUSION

In this paper, the recently measured quasi-elastic and inelastic scattering of the $^{20}\text{Ne} + ^{130}\text{Te}$ system at $15.3A$ MeV is analyzed using the optical nuclear model. The real part of the nuclear potential is generated using three

Table 2. Best fit parameters required for the DWBA and CC calculations of CPM1. The parameters N_R , r_W , and a_W are fixed as in Table 1.

Nucleus	Technique	W_0/MeV	δ_2^{corr}	χ^2	σ_R/mb
$^{20}\text{Ne} (2^+)$	DWBACC	11.259.02	1.301.30	43.4511.15	34743537
$^{130}\text{Te} (2^+)$	DWBACC	11.4910.43	0.740.74	13.9213.41	34833492
$^{130}\text{Te} (4^+)$	CC	10.66	0.33	95.6	3500
$\text{Ne}_{1.633}^{+2} + \text{Te}_{0.839}^{+2}$	CC	14.74	1.300.74	4.18	3728

folding optical potentials. First, the potential CPM1 is generated using the cluster structure of the projectile ^{20}Ne as $\alpha + ^{16}\text{O}$ in a similar manner to our previous work [44]. The second potential CPM2 is derived using the 5α cluster structure of the ^{20}Ne . Finally, a potential based on the effective CDM3Y6 Paris NN interaction is constructed for comparison. The imaginary potentials are used as a phenomenological WS form. In the calculations of the elastic scattering cross-sections, only the free parameter (W_0) is considered while maintaining the normalization factor $N_R=1$, imaginary potential radius $r_w = 1.40$, and diffuseness $a_w = 0.55$. The calculated elastic scattering angular distribution using the derived semi-microscopic OMPs in a simple one-channel has a reasonable agreement with the experimental data of quasi-elastic scattering. This result may be related to the cluster structure ($\alpha + ^{16}\text{O}$) of ^{20}Ne , which can contribute to the deformation of the nucleus geometric structure. In the second step of the calculations, the experimental data for quasi-elastic and inelastic scattering are analyzed using the DWBA and CC technique within the rotational model. The cross section of the inelastic state is obtained with the DP of the semi-microscopic CPM1 with the same optimization procedure employed in the elastic calculations. This potential is selected because it was confirmed to be appropriate and successful in describing the same data in the same energy range [44].

The transitions of the ^{20}Ne projectile 2^+ excited state at 1.633 MeV and 4^+ excited state for ^{130}Te are considered to analyze the experimental cross section angular distribution with the peak ≈ 1.6 MeV visible in the $^{20}\text{Ne} + ^{130}\text{Te}$ spectrum. A satisfactory agreement between the theoretical calculations and experimental data is attained when the full coupling effects are explicitly considered in the CC approach. The obtained CC results reveal that the

inclusion of 2^+ state of ^{20}Ne has the strongest influence and is sufficient to reproduce the experimental data at this energy region. This result is compatible with the conclusion of Ref. [25].

The cross section with the third peak (≈ 2.5 MeV) in the spectrum is obtained with the $\text{Ne}_{1.633}^{+2} + \text{Te}_{0.839}^{+2}$ transition in the CC calculations. The calculated angular distribution cross section using the CC potential in this work is fitted the experimental data more than that obtained in Ref. [25].

The cluster model for ^{20}Ne within the semi-microscopic potential CPM1, in addition to the limited one free parameter, has an acceptable agreement with the considered experimental data. Moreover, the effect of excited-state contributions appears in the backward angles. This confirms the success of the present model similar to those obtained in the previous work [25] that used the microscopic SPP with nucleonic densities (two Fermi parameters).

In conclusion, the potentials calculated in this work can describe the experimental data under study in this range of energies and produce results corresponding with the only available study [25]. The obtained results demonstrate the ability of the $\alpha + ^{16}\text{O}$ cluster model of ^{20}Ne in analyzing the DCE reactions [44]. In addition, some new quantities, such as σ_R and J_R require additional theoretical studies in this field. This will enable more comparisons to obtain the best potentials and results that can contribute to this project.

ACKNOWLEDGMENTS

The authors are grateful to Roberto Linares for supporting us with the experimental data for the studied nuclear system.

References

- [1] C. Agodi, F. Cappuzzello, M. Cavallaro *et al.*, *Nucl. Part. Phys. Proc.* **265**, 28 (2015)
- [2] F. Cappuzzello, C. Agodi, M. Cavallaro *et al.*, *Eur. Phys. J. A* **54**, 72 (2018)
- [3] W. C. Haxton and G. J. Stephenson, *Prog. Part. Nucl. Phys.* **12**, 409 (1984)
- [4] T. Tomoda, *Rep. Prog. Phys.* **54**, 53 (1991)
- [5] J. Suhonen and O. Civitarese, *Phys. Rep.* **300**, 123 (1998)
- [6] J. D. Vergados, H. Ejiri, and F. Simkovic, *Rep. Prog. Phys.* **75**, 106301 (2012)
- [7] E. -W. Grewe and D. Frekers, *Prog. Part. Nucl. Phys.* **57**, 260 (2006)
- [8] A. S. Barabash, *Nucl. Phys. A* **935**, 52 (2015)
- [9] F. Cappuzzello, M. Cavallaro, C. Agodi *et al.*, *Eur. Phys. J. A* **51**, 1 (2015).
- [10] J. Barea, J. Kotila, and F. Iachello, *Phys. Rev. Lett.* **109**, 042501 (2012)
- [11] E. Majorana, *Nuovo Cim.* **14**, 171 (1937)
- [12] S. Dell’Oro, S. Marocci, M. Viel *et al.*, *Adv. High Energy Phys.* **2016**, 2162659 (2016)
- [13] M. Dolinski, A. Poon, and W. Rodejohann, *Annu. Rev. Nucl. Part. Sci.* **69**, 219 (2019)
- [14] G. Collaboration, M. Agostini, G. R. Araujo *et al.*, *Phys. Rev. Lett.* **125**, 252502 (2020)
- [15] H. Ejiri, J. Suhonen, and K. Zuber, *Phys. Rep.* **797**, 1 (2019)
- [16] H. Ejiri, *Universe* **6**, 225 (2020)
- [17] J. Menéndez, *J. Phys. G Nucl. Part. Phys.* **45**, 14003 (2017)
- [18] F. Cappuzzello, C. Agodi, M. Bondi *et al.*, *J. Phys. Conf. Ser.* **630**, 12018 (2015)
- [19] M. Cavallaro and others, *PoS BORMIO 2017*, 15 (2017)
- [20] C. Agodi, F. Cappuzzello, D. L. Bonanno *et al.*, *AIP Conf. Proc.* **1686**, 020001 (2015)
- [21] C. Agodi, A. D. Russo, L. Calabretta *et al.*, *Universe* **7**, 72 (2021)
- [22] K. Kisamori, S. Shimoura, H. Miya, S. Michimasa *et al.*, *Phys. Rev. Lett.* **116**, 52501 (2016)
- [23] H. Matsubara, M. Takaki, T. Uesaka *et al.*, *Few-Body Syst.* **54**, 1433 (2013)

- [24] V. Soukeras, L. Acosta, C. Agodi *et al.*, *J. Phys. : Conf. Ser.* **2619**, 012016 (2023)
- [25] D. Carbone, R. Linares, P. Amador-Valenzuela *et al.*, *Universe* **7**, 58 (2021)
- [26] V. Soukeras, F. Cappuzzello, D. Carbone, M. Cavallaro *et al.*, *Results Phys.* **28**, 104691 (2021)
- [27] M. Cavallaro, G. Santagati, F. Cappuzzello, D. Carbone *et al.*, *Results Phys.* **13**, 102191 (2019)
- [28] V. Albanese, R. Alves, M. R. Anderson *et al.*, *J. Instrum.* **16**, P08059 (2021)
- [29] H. Lenske, *J. Phys. Conf. Ser.* **1056**, 12030 (2013)
- [30] H. Lenske, J. I. Bellone, M. Colonna *et al.*, *Phys. Rev. C* **98**, 044620 (2018)
- [31] M. Colonna, J. I. Bellone, S. Burrello *et al.*, *Cern Proc.* **1**, 77 (2019)
- [32] D. Q. Adams, C. Alduino, K. Alfonso *et al.*, *Nature* **604**, 53 (2022)
- [33] Z. M. M. Mahmoud and M. A. Hassanien, *Phys. At. Nucl.* **82**, 599 (2019)
- [34] K. O. Behairy, M. El-Azab Farid, A. A. Ibraheem *et al.*, *Chin. Phys. C* **45**, 24101 (2021)
- [35] M. Anwar, *Phys. Rev. C* **101**, 64617 (2020)
- [36] K. O. Behairy and T. H. Alsheddi, *J. Phys. Soc. Japan* **91**, 124201 (2022)
- [37] M. Anwar, B. El-Naggar, and K. O. Behairy, *J. Phys. Soc. Japan* **91**, 14201 (2022)
- [38] M. A. Hassanain, A. A. Ibraheem, S. M. M. Al Sebiey *et al.*, *Phys. Rev. C* **87**, 034601 (2013)
- [39] M. E. -A. Farid, Z. M. M. Mahmoud, and G. S. Hassan, *Nucl. Phys. A* **691**, 671 (2001)
- [40] M. A. Hassanain, A. A. Ibraheem, and M. E. -A. Farid, *Phys. Rev. C* **77**, 034601 (2008)
- [41] M. A. Hassanain, M. Anwar, and K. O. Behairy, *Phys. Rev. C* **97**, 044610 (2018)
- [42] Z. M. M. Mahmoud and K. O. Behairy, *Brazilian J. Phys.* **47**, 189 (2017)
- [43] M. E. A. Farid, *Phys. Rev. C* **65**, 67303 (2002)
- [44] A. Hemmdan, M. A. Hassanain, M. Anwar *et al.*, *Phys. Rev. C* **104**, 044604 (2021)
- [45] B. Buck, C. B. Dover, and J. P. Vary, *Phys. Rev. C* **11**, 1803 (1975)
- [46] B. Buck, J. C. Johnston, A. C. Merchant *et al.*, *Phys. Rev. C* **52**, 1840 (1995)
- [47] B. Buck, A. C. Merchant, and S. M. Perez, *Phys. Rev. C* **51**, 559 (1995)
- [48] Y. A. Bereznoy and V. P. Mikhailyuk, *Phys. At. Nucl.* **63**, 715 (2000)
- [49] D. T. Khoa, W. von Oertzen, and H. G. Bohlen, *Phys. Rev. C* **49**, 1652 (1994)
- [50] D. T. Khoa, G. R. Satchler, and W. von Oertzen, *Phys. Rev. C* **56**, 954 (1997)
- [51] G. R. Satchler and W. G. Love, *Phys. Rep.* **55**, 183 (1979)
- [52] M. N. El-Hammamy, A. A. Ibraheem, and S. Hamada, *J. Taibah Univ. Sci.* **18**, 2330129 (2024)
- [53] Z. M. M. Mahmoud, A. Hemmdan, and K. O. Behairy, *Results Phys.* **16**, 102892 (2020)
- [54] H. De Vries, C. W. De Jager, and C. De Vries, *At. Data Nucl. Data Tables* **36**, 495 (1987)
- [55] G. L. Zhang, H. Liu, and X. Y. Le, *Chin. Phys. B* **18**, 136 (2009)
- [56] D. T. Khoa, N. H. Phuc, D. T. Loan *et al.*, *Phys. Rev. C* **94**, 34612 (2016)
- [57] G. R. Satchler, *Direct Nuclear Reactions* (Oxford: Oxford University Press, 1983)
- [58] B. Pritychenko, M. Birch, B. Singh *et al.*, *At. Data Nucl. Data Tables* **107**, 1 (2016)
- [59] A. Hemmdan, M. A. Hanssanian, M. Anwar *et al.* (unpublished)
- [60] D. T. Khoa, Computer program DFPD4 (private communication).
- [61] I. J. Thompson, *Comput. Phys. Reports* **7**, 167 (1988)
- [62] A. Spatafora, F. Cappuzzello, D. Carbone *et al.*, *Phys. Rev. C* **100**, 34620 (2019)